

A portable modeler of lensed quasars

Prasenjit Saha

*Astronomy Unit
Queen Mary and Westfield College
University of London
London E1 4NS, UK*

`p.saha@qmul.ac.uk`

and

Liliya L.R. Williams

*Department of Astronomy
University of Minnesota
116 Church Street SE
Minneapolis, MN 55455*

`llrw@astro.umn.edu`

ABSTRACT

We introduce and implement two novel ideas for modeling lensed quasars. The first idea is to require different lenses to agree about H_0 . This means that some models for one lens can be ruled out by data on a different lens. We explain using two worked examples. One example models 1115+080, 1608+656 (time-delay quads) and 1933+503 (a prospective time-delay system) all together, yielding time-delay predictions for the third lens and a 90%-confidence estimate of $H_0^{-1} = 14.6_{-1.7}^{+9.4}$ Gyr ($H_0 = 67_{-26}^{+9}$ km s $^{-1}$ Mpc $^{-1}$) assuming ($\Omega_M = 0.3, \Omega_\Lambda = 0.7$). The other example models the time-delay doubles 1520+530, 1600+434, 1830-211, and 2149-275, which gives $H_0^{-1} = 14.5_{-1.5}^{+3.3}$ Gyr ($H_0 = 67_{-13}^{+8}$ km s $^{-1}$ Mpc $^{-1}$). Our second idea is to write the whole modeling software as a highly interactive Java applet, which can be used both for coarse-grained results inside a browser and for fine-grained results on a workstation. Several obstacles come up in trying to implement a numerically-intensive method thus, but we overcome them.

Subject headings: gravitational lensing

1. Introduction

Some aspects of modeling lensed quasars are much as they were just after the discovery of the first double quasar 0957+561. In one of the earliest lens-modeling papers, Young et al. (1981) are concerned with some now-very-familiar issues: the effect on image positions of both the main lensing galaxy and other galaxies, the time delays predicted by the models, the non-uniqueness of the models despite the adequacy of the data, and the desirability of supplementary data about the lens, such as velocity dispersions or X-rays.

But other aspects of the subject these days would have been unimaginable in 1981. The first double quasar has been joined by dozens of others: the CASTLES survey compilation (Kochanek et al. 1998) currently lists 76 secure multiple-image galaxy-lens systems, with image positions measured to the mas level, even more precisely if there are compact radio sources. And the time delay for 0957+561, for which Young et al.’s preliminary estimate was about 5 years, is now measured as 423 ± 1 days (Osoz et al. 2001), along with time-delay measurements for eight other systems (Schechter et al. 1997; Lovell et al. 1998; Biggs et al. 1999; Burud et al. 2000; Cohen et al. 2000; Burud et al. 2002a,b; Fassnacht et al. 2002; Hjorth et al. 2002).

These excellent data demand new, more automatic, and more portable software tools for modeling the lenses. Thus motivated, we have developed a new code, *PixeLens*, which we present in this paper.

PixeLens works by reconstructing a pixelated mass map for the lens, an idea we first implemented in Saha & Williams (1997). Most lens modeling codes work by fitting a parametric functional form—for example, Young et al. (1981) fitted King models; *gravlens* by Keeton (2001) is a modern example, offering the user a large choice of parametric models. There are other possibilities too: Trotter et al. (2000) reconstruct lenses non-parametrically as we do, but use multipole expansions rather than pixels.

PixeLens generates large ensembles of models rather than one or a few mass maps, as a way of addressing the non-uniqueness problem. We introduced this strategy in Williams & Saha (2000) for pixelated models. Keeton & Winn (2003) use a somewhat similar strategy, but with parametrized models.

But *PixeLens* also brings two completely new features, one astrophysical, one computational:

- It can model several lenses simultaneously, enforcing consistency of H_0 across different time-delay lenses. As a result, lenses can be used to constrain other lenses in an interesting and surprising way;
- The code is highly portable and can run without change as a standalone program, or as a Java applet inside a web browser. In the online version of this paper, it is available as an alternative version of Figure 1.

The best way to explain what we have implemented and what problems remain is through an example. So in the following section we will work through a simultaneous reconstruction of three lenses: the time delay quads 1115+080 and 1608+656, and the ten-image system 1933+503. This will be the main part of the paper. We turn to some computational issues after that.

2. A worked example: reconstructing three lenses

In our first worked example, we consider the three lenses currently best-constrained by observations.

1. 1115+080 is a quad where the lens is an elliptical galaxy supplemented by external shear from other group galaxies. It was the second lens to be discovered (Weymann et al. 1980). Schechter et al. (1997), together with an improved time-series analysis by Barkana (1997) provide time-delays between two pairs of images.
2. 1608+656 is a quad with the lens being apparently two interacting galaxies. It was discovered (Myers et al. 1995) in the CLASS survey. There are time delays between all pairs of images (Fassnacht et al. 2002).
3. 1933+503 is really two quads and a double. The lens appears to be an elliptical, but the source is a radio source with a core and opposing lobes. The core and one of the lobes are imaged as quads while the other lobe is imaged as a double. It was also discovered in the CLASS survey (Sykes et al. 1998). There are no measured time-delays, but there are prospects for time delays from the core quad. We will predict time delays for the core quad.

The CASTLES web page provides further information. We can also make some preliminary inferences about the lenses by examining the morphology, as explained in Saha & Williams (2003): we can work out the time-ordering of each of the image systems, and for 1115+080 we can recognize an external shear and its approximate axis.

Let us now proceed to apply *PixeLens*. Figure 1 shows the user interface, which we will explain in stages below.

2.1. The data input

Data is entered by typing into the ‘data area’. (There is also an ‘input paste’ feature with a number of example inputs, which can be pasted and then edited by selecting the ‘edit’ option of the menu.)

For 1115+080, we enter the following.

```
object 1115
symm pixrad 12 maprad 2
redshifts 0.311 1.722
shear -45
quad
  0.3550  1.3220
-0.9090 -0.7140 13.3
-1.0930 -0.2600 0
  0.7170 -0.6270 11.7
```

The first line just labels the object. The second line specifies that the mass maps be inversion-symmetric with a radius of $2''$ and 12 pixels (thus setting the pixel size). The fourth line gives the approximate shear axis (`shear 135` would be equivalent), in degrees relative to East. The program will consider positions angles within 45° of what is given. The last four lines give the image positions (in arcseconds and relative to the lens center) and the time delays (in days and relative to the previous image). The images must be ordered by arrival-time. The ‘0’ in the second-last line means that the time-delay is > 0 but unknown. Otherwise, uncertainties in image positions and time delays are assumed negligible.

Note how the input format assumes that some preliminary analysis, of the qualitative variety explained in Saha & Williams (2003) has already been done.

For 1608+656 we enter the following.

```
object 1608
pixrad 9 maprad 2
redshifts 0.630 1.394
quad
-1.300 -0.800
-0.560  1.160 31
-1.310  0.700  5
  0.570 -0.080 40
```

The format is just as before, except that we have left out `symm`, because the lens here appears to be asymmetric.

For 1933+503 we enter the following.

```
object 1933
symm pixrad 10
redshifts 0.76 2.63
shear 45
quad -0.40  0.53  0.43 -0.26 0
      0.40  0.19 0 -0.19 -0.33 0
quad  0.54 -0.44 -0.15  0.44 0
      -0.03  0.45 0 -0.38 -0.12 0
double -0.47  0.60  0.13 -0.30 0
```

Here we have left out the mass-map radius, leaving the program to choose it. We have also given image data on two quads and a double rather than just one quad, and indicated unknown time delays with many 0s. Line breaks in the input have no significance.

Figure 2 summarizes the image data and the pixelation. (For symmetric mass maps, only half the pixels are shown here, the other half are specified by inversion symmetry.) *PixeLens* produces such plots before starting the real computations, and they provide a convenient goof test on the input.

Now we type

```
models 100
```

in the ‘data area’ and click on the ‘run’ button, and away we go.

2.2. Generating an ensemble of models

At this point, we recall some lensing theory. For a source at $\vec{\beta}$, the arrival-time at $\vec{\theta}$ is

$$\tau(\vec{\theta}) = \frac{1}{2}|\vec{\theta}|^2 - \vec{\theta} \cdot \vec{\beta} - \int \ln |\vec{\theta} - \vec{\theta}'| \kappa(\vec{\theta}') d^2\vec{\theta}' \quad (1)$$

where κ is the dimensionless density (also called convergence). If we measure angles in arcsec, τ will have units of arcsec². To turn it into days we have to multiply by $gT(z_L, z_S)$, where T is a time scale and g is H_0^{-1} in Gyr (see Appendix A). In addition to the indicated redshift dependence, $T(z_L, z_S)$ has a weak cosmology dependence. By default *PixeLens* assumes $\Omega_M = 0.3, \Omega_\Lambda = 0.7$, which gives $T^{1115} = 3.34$ days, $T^{1608} = 10.28$ days, and $T^{1933} = 9.72$ days.

In our models, the mass is pixelated. Therefore we can simplify Equation (1) to

$$\tau(\vec{\theta}) = \frac{1}{2}|\vec{\theta}|^2 - \vec{\theta} \cdot \vec{\beta} - \sum_n \kappa_n Q_n(\vec{\theta}) \quad (2)$$

where κ_n is the density on the n -th pixel and $Q_n(\vec{\theta})$ is the integral from (1) evaluated over that pixel. The explicit form of $Q_n(\vec{\theta})$ is a messy but straightforward mixture of logs and arctans and is given in Saha & Williams (1997). The important thing about Equation (2) is that it is linear in the unknowns, $\vec{\beta}$ and κ_n . We also allow a constant external shear

$$\gamma_1(\theta_x^2 - \theta_y^2) + 2\gamma_2\theta_x\theta_y \quad (3)$$

to be added to Equation (2); again, the shear is linear in the unknowns γ_1, γ_2 .

We now implement the following observational constraints.

1. An image observed at $\vec{\theta}_i$ implies

$$\vec{\nabla}\tau(\vec{\theta}_i) = 0. \quad (4)$$

In a multiple-image system all the images have the same unknown $\vec{\beta}$, so each multiple-image system introduces $2([\text{images}] - [\text{sources}])$ constraints. Thus a double provides 2 image constraints, a quad 6, while 1933+503 provides 14.

2. A time-delay measurement between images at $\vec{\theta}_i$ and $\vec{\theta}_j$ implies

$$\tau(\vec{\theta}_i) - \tau(\vec{\theta}_j) = \frac{[\text{obs delay}]}{g T(z_L, z_S)}. \quad (5)$$

Here g is another unknown and, fortunately for us, g^{-1} appears linearly. If a time-delay is unmeasured, but we are sure about the ordering, we replace (5) by an inequality constraint

$$\tau(\vec{\theta}_i) - \tau(\vec{\theta}_j) \geq 0. \quad (6)$$

We have 3 equality constraints from time delays in 1608+656, 2 in 1115+080, and none in 1933+503.

3. We require the images to have the expected parities, and for the image elongation when projected along the radial direction to be between $\frac{1}{10}$ and 10. Although very modest, these requirements do suppress a tendency for spurious images to be created in the vicinity of a nearly-merging pairs of genuine images. Constraints of this type are also linear (AbdelSalam et al. 1998).
4. We remarked after Equation (5) that g is an unknown variable in the constraint equations. Now, if we write the constraint equations for several lenses, then each lens will introduce a separate unknown variable for g , say g^{1115} , g^{1608} and so on. But g is universal, so we have additional constraint equations of the type

$$g^{1115} = g^{1608}, \quad g^{1608} = g^{1933}. \quad (7)$$

Though g is still unknown, it now couples the constraint equations for different lenses. This coupling is the central astrophysical contribution of this paper. In particular, it means that if one lens rules out a certain range of g , *PixeLens* will not consider models of any lens that require g in that range.

We also impose secondary constraints based on our general knowledge of galaxy mass profiles.

1. All the $\kappa_n \geq 0$,
2. If the galaxy does not appear very asymmetric, the mass profile is required to have inversion symmetry about the lens center.
3. The density gradient anywhere must point within $\leq 45^\circ$ of the lens center. The precise formulation of this constraint is given in Saha & Williams (1997).
4. The κ_n of any pixel must be ≤ 2 [average of neighbors], except for the central pixel, which is allowed to be arbitrarily dense.
5. The radial mass profile must be steeper than $|\vec{\theta}|^{-0.5}$. The stellar dynamical evidence indicates that the total density distribution in the central regions of ellipticals is well approximated by isothermal, r^{-2} (Rix et al. 1997; Gerhard et al. 2001), while the study of the dynamics of the gas in the center of our Galaxy show that total density scales as $r^{-1.75}$ (Binney et al. 1991). Guided by these studies we choose $|\vec{\theta}|^{-0.5}$ as a conservative minimal steepness of the 2D density profiles in galaxies.

In Bayesian terminology, these secondary constraints constitute a prior.

The observational and prior constraints confine allowed lenses to a polyhedron in the space of $(\kappa_1, \kappa_2, \dots, \kappa_N, \vec{\beta})$. *PixeLens* searches this polyhedron by a Monte-Carlo technique, briefly explained in Figure 3. The key idea is to random-walk between models such that probability of moving from model *A* to model *B* equals the probability of moving from model *B* to model *A*. This is a simple example of a Metropolis algorithm, or a Markov-chain Monte-Carlo method. Generalizations to non-uniform priors are also possible—see, for example, Saha (2003).

In our example, each model that *PixeLens* generates is a three-lens model: there are mass maps, external-shear models where required, and inferred source positions for each of 1115+080, 1608+656, and 1933+503. In any one model the lenses are coupled by a common value of *g*, but different models may have different values of *g*.

As soon as the first model is ready, the user can examine it. But the users will not want to examine every model in an ensemble of 100. So *PixeLens* presents two kinds of results from the ensemble: details of the average model of the ensemble-so-far and various statistics derived from the ensemble. (By ensemble-average model we mean a model with the densities in each pixel, the source positions, and any external shear averaged over the ensemble. The constraint equations being linear in the quantities being averaged, they are still satisfied by ensemble averages.) Let us consider the two kinds of results in turn.

2.3. Results: the ensemble-average model

Figure 4 shows mass maps for the three lenses from the ensemble-average model. For 1115+080 and 1608+656, the mass maps are very similar to those in Williams & Saha (2000). The modeling method and input data in the earlier paper were very similar—except for the coupling (7)—but the code was completely different. We remark that the elongation of the mass profiles in 1115+080 is towards the other group galaxies, the elongations in 1608+656 and 1933+503 are what we might expect from the light in those lenses.

Figure 5 shows the lens potential in 1115+080. (The default is to pick the contours that pass through the images, but the user can try different contour spacings interactively, by typing in the appropriate values in the ‘plot parameters’ boxes.) Notice how smooth the potential is: nothing of the pixelation so evident in the mass maps is visible here; it has been washed out by the double integral in Equation (1).

Figure 5 also illustrates a convenient way of gauging the importance of external shear in a model. *PixeLens* allows the user to plot the lens potential with the external shear exaggerated. (Such exaggeration is purely for visualization, it has no effect on the models.) The user can adjust an exaggeration parameter: the default is 1, while 0 means omit the external shear. Figure 5 shows that a 3-fold exaggeration makes a drastic difference to the potential, indicating that the external shear in this lens is large but not dominant.

Figure 6 show saddle-point contours in the arrival-time surfaces for the two quads and a double of 1933+503. Saddle-point contours are the default, but as with the potential, the user can try different contour spacings interactively. Examining the arrival-time contours is a very good way of checking that the model is sensible: small errors in the input or the modeling code nearly always lead to noticeable spurious features in the arrival-time surface, such as contorted contours or extra images.

Arrival-time contours also have another, somewhat surprising, use. Figure 7 shows the result if the user specifies a contour-spacing of 0.004. (The units here are arcsec^2 . We can convert to physical time units, as explained after Equation 1, and the result is about 5 hr, but let us continue with arcsec^2 .) A plot of the arrival-time surface with closely-spaced contours tends to resemble an Einstein ring. In fact, it approximates—see Saha & Williams (2001) for details—the image of a source with a conical light profile of radius

$$\frac{[\text{contour spacing}]}{[\text{thickness of contour lines}]}. \quad (8)$$

Now, the line thickness in all the plots in this paper is $\frac{1}{300}$ of the plot width. For Figure 7, that amounts to $\simeq 0.015''$. Hence Figure 7 predicts the image due to a conical profile of radius $\simeq 0.33''$ centered on the QSO. In fact it resembles the ring imaged by Impey et al. (1998), though there are differences of detail. Thus, we can make quantitative inferences about the host galaxy simply by inspecting images and doing some mental arithmetic.

2.4. The model ensemble: stats

Out of the full ensemble of models, it is possible to extract many kinds of statistics. *PixeLens* implements four kinds, all involving H_0^{-1} .

Figure 8 shows a histogram of g values from the ensemble, and has a straightforward interpretation as the posterior distribution of H_0^{-1} . This figure is analogous to Figure 17 in Williams & Saha (2000), but better. In the earlier work we had separate model ensembles for 1115+080 and 1608+656 and multiplied their h -histograms bin-by-bin. That procedure had the problems of (i) a reduced number of models in the common region, and (ii) increased shot noise from bin-by-bin multiplication. In *PixeLens*, because of the constraint (7), there is only one histogram of g , which eliminates both problems. This histogram (or rather, the unbinned values it represents) gives

$$\begin{aligned} H_0^{-1} &= 14.6_{-1.2}^{+3.8} \text{ Gyr} \quad (H_0 = 67_{-14}^{+6} \text{ local units}) \quad \text{at 68\% confidence} \\ H_0^{-1} &= 14.6_{-1.7}^{+9.4} \text{ Gyr} \quad (H_0 = 67_{-26}^{+9} \text{ local units}) \quad \text{at 90\% confidence.} \end{aligned}$$

The median H_0 is somewhat higher than in Williams & Saha (2000), but this is expected because that paper used an Einstein-de-Sitter cosmology, which shortens $T(z_L, z_S)$ by $\sim 5\%$ for 1115+080 and by $\sim 10\%$ for 1608+656. The uncertainties are similar.

Figure 9 shows the predicted time-delays for the core-quad in 1933+503.

Figure 10 shows the radial index α from a radial fit of $|\vec{\theta}|^{-\alpha}$ against g^{-1} . Most lens systems when modeled independently show a correlation between α and g^{-1} (or h), in the sense that steeper density profiles result in higher values of h (e.g., Figure 13a and 16a of Williams & Saha 2000). For the three coupled lenses shown here, 1115+080 shows the correlation weakly and the others hardly at all.

Figure 11 shows the mean κ in the annulus between the innermost and outermost images (say $\langle \kappa \rangle_{\text{ann}}$) against g^{-1} . Again, when modeled independently, most lens systems show an anti-correlation between $\langle \kappa \rangle_{\text{ann}}$ and g^{-1} , whereas two of the three panels of Figure 11 show no trends at all. This can be expected, because coupling different time-delay systems weakens correlations: coupling reduces the range of g explored, and over a reduced range of g any correlation involving g will appear weaker. For an extreme case, suppose we artificially fix the value of g , which we can do by adding (say)

$$g = 14$$

at the end of the input. Then Figures 10 and 11 will consist of vertical clusters of point at $g = 14$.

However, the above argument does not fully account for the lack of trends in the middle and lower panels of Figure 11; other causes are partially responsible. Kochanek (2002) derives a linear relation between time delay, $\langle \kappa \rangle_{\text{ann}}$, and h , as a leading order approximation from lensing theory. If one of these three (sets of) variables is fixed, say if the time delays are fixed by observations, then a well defined trend would be expected to relate the other two ($\langle \kappa \rangle_{\text{ann}}$ and h). This is demonstrated

by 1115+080. 1933+503, on the other hand, is not expected to exhibit such a trend because no time delays exist for this system. Finally, 1608+656 shows no trend probably because it is a distinctly asymmetric lens.

2.5. Artifacts

To finish this worked example, we remark on some artifacts evident in pixelated models.

The most obvious spurious feature is the pixel-scale substructure. In principle, one could replace mass pixels with basis functions, thereby preserving the linearity of the constraint equations and leaving the main algorithms unchanged, but making the mass maps smooth. That would be a useful development for microlensing applications, where local density and shear are crucial. But for studying image positions and time delays, basis functions are unlikely to make any difference, because the pixel scale structure is completely suppressed in the lens potential and arrival time—see Figure 5.

Pixelation has a serious side-effect, however, if the pixels are made too large. We have found from experimenting with different pixel sizes that if the pixels are too large and the mass-distribution is poorly resolved, fewer steep mass-models are allowed. As a result, the prior is shifted to favor lower values of g^{-1} , and hence the Hubble-time histograms also shift towards larger H_0^{-1} . The effect is most noticeable in the α - g^{-1} correlation. The pixel-sizes used for this paper are chosen small enough not to cause this particular problem.

A second artefact concerns the central image. Now the central maximum itself is obvious from arrival time contour maps. What is further often evident is that the central maximum is slightly offset from the lens center and not as steep as expected from the practical unobservability. This happens because our mass maps lack a central density cusp, instead distributing the mass over the central pixel. In principle, we could incorporate central density cusps into *PixeLens*. But it would make no difference to the observed images because, as is well known, a circular mass disk has the same lensing effect outside itself as a point mass.

A third (and rare) artefact is spurious extra images. The density-gradient constraint, we have found, is generally enough to suppress extra images, but it is possible that a few rogue models with spurious extra images are present in the ensembles. In principle we could reject those models by examining every single arrival-time surface by eye, but we have not implemented that.

3. A complementary worked example: four lenses

In our second example we will be more brief.

We reconstruct four time-delay doubles.

- 1520+530 was discovered by Chavushyan et al. (1997) and Burud et al. (2002b) measured its time-delay.
- 1600+434 was discovered by Jackson et al (1995) and Burud et al. (2000) measured its time delay.
- 1830-211 was discovered by Rao & Subrahmanyam (1988) and Lovell et al. (1998) measured its time delay.
- 2149-275 was discovered by Wisotzki et al (1996) and Burud et al. (2002a) measured its time delay.

3.1. The data input

We have already explained the input format, and without further ado here are the data we input.

```
object 1520
symm pixrad 8 redshifts 0.71 1.855 shear 90
double 1.141 0.395 -0.288 -0.257 130
object 1600
symm pixrad 8 redshifts 0.42 1.59
double 0.610 0.814 -0.110 -0.369 51
object 1830
symm pixrad 8 redshifts 0.89 2.51
double -0.50 0.46 0.15 -0.26 26
object 2149
symm pixrad 8 redshifts 0.490 2.03
double 0.736 -1.161 -0.173 0.284 103
```

We can omit the number of models since 100 is the default.

In the case of PKS 1830-211, the position of the lensing galaxy at $z = 0.89$ remains uncertain. Various scenarios have been proposed in the literature (Lehar et al. 2000; Winn et al. 2002; Courbin et al. 2002; Koopmans & de Bruyn 2003); we use the astrometry from Lehar et al. (2000).

3.2. Results

Since readers will have already seen the various kinds of results possible, we now give only a small selection.

Figure 12 shows the ensemble-average mass maps.

Figure 12 shows the common histogram of Hubble times, from which we obtain

$$\begin{aligned} H_0^{-1} &= 14.5^{+1.6}_{-1.1} \text{ Gyr} \quad (H_0 = 67^{+6}_{-7} \text{ local units}) \quad \text{at 68\% confidence} \\ H_0^{-1} &= 14.5^{+3.3}_{-1.5} \text{ Gyr} \quad (H_0 = 67^{+8}_{-13} \text{ local units}) \quad \text{at 90\% confidence} \end{aligned}$$

Figure 14 shows $\langle \kappa \rangle_{\text{ann}}$ against g^{-1} for the four doubles. All four show a correlation, 1600+434 being the best. These correlations are somewhat worse compared to what they would have looked like if the lens systems were modeled independently (as the reader can readily verify using *PixeLens*): as explained in Section 2.4, coupling lens systems weakens the correlations.

4. Computational issues: reconciling portability and efficiency

The first decision we made about *PixeLens* was to write it in Java. The overriding consideration was portability: we wanted to code to run without modification on a high-end workstation, a laptop computer used during a talk, or inside a web browser. While developing the software we also found other advantages of Java. For example, the graphics libraries are part of the standard, making GUIs very easy to write. Also, the language is remarkably clean¹ and easy to debug.

But these advantages come at a price, and we found there were four issues we had to confront.

First, Java still lacks compilers optimized for numerical work. Java numerical code runs slower than C++ by a factor of 3 or more, and also takes up more memory. This is an annoying inconvenience, but it is not fatal. (Given Moore’s law, it is like running C++ on a two-year-old computer.)

Second, there is very little support for scientific programming. In particular, in all the elaborate Java graphics libraries, there is no simple package to do a plot of x against y ! In response, we just wrote whatever utility software we needed. For example, we wrote Java code to generate PostScript code to draw the big and small ticks in an x, y plot. But this utility code is now available for other projects and to other researchers.

Third, disk input/output is not allowed from inside a web browser. This is an essential security precaution—clearly, untrusted code running over the internet must not be allowed disk access. Fortunately, the language allows an elegant workaround. *PixeLens* checks whether it is running inside a web browser or as a standalone program (as an applet or an application in the jargon) and activates disk input/output only in the latter case. So users can try the code out over the internet inside a web browser; if they are interested enough to want disk output, they can download and run like a normal program.

Fourth, and most importantly, there is no batch mode inside a web browser. If the program takes more than a few seconds to produce results, which user will want to wait in front of their web

¹Apart from a culture of capital letters inside words, which made the name *PixeLens* inevitable.

browser? This seems to us the fundamental reason why numerically-intensive Java programs were previously unknown. One can write such programs and run them in batch mode in the normal way, but if they are useless inside a web browser the single largest advantage of Java is lost. But there is a way out. That way is to provide the user with intermediate results, and the means to post-process them in non-trivial ways, while the main computation is still running. With *PixeLens*, the user can start examining the results as soon as the first model of the ensemble is complete, even though only 1% of the total computation may have run. We found that providing the user with intermediate results and sufficient flexibility to make them interesting influenced almost every aspect of our program design.

PixeLens is internally documented in a literate programming idiom (Knuth 1992) and we will not enter into minutiae here, but Figure 15 gives a general idea of how the code is organized. Imagine each of the labelled ovals as consisting of many variables and several functions that can operate on those variables. Functions from one oval may know something about the variables and functions of another oval, but only the bare minimum needed to work together.

(Text I/O) is the simplest of the ovals. It accepts the data and other input like ‘run’ and ‘pause’, and outputs diagnostics and error messages, but does not interpret the input itself. (Router) interprets enough of the input to work out how many lenses there are, allocates the required number of (Lens) ovals—two in Figure 15—and passes the data to them. The (Lens) ovals are the only parts that know about lensing theory and pixelation. Each of them turns the data into constraint equations. (Router) then takes the constraint equations from each (Lens), packs them into one large set of equations, and gives them to (Simplex). (Simplex) generates solutions using linear programming and Monte-Carlo, and it does nearly all the numerical work involved. Each time a new solution is ready, (Simplex) passes it to (Router), which unpacks it and distributes among the (Lens) ovals. Each (Lens) oval then post-processes the solution, preparing grids of κ and $\tau(\vec{\theta})$ and so on. The post-processed material is passed via (Router) to (Graphics I/O). (Graphics I/O) can interact with the user and do some non-trivial computation on its own: it can make contour plots, scatter plots, and histograms to the user’s specification, all without needing to know any lensing theory. Moreover (Graphics I/O) can work without interrupting (Simplex) or the other ovals, even for error-recovery. In effect, model generation happens in the background while the user examines intermediate results in the foreground.

5. Conclusions

This paper continues our work on modeling lens quasars using pixelated mass maps. We elaborate on ideas introduced in earlier papers (Saha & Williams 1997; Williams & Saha 2000; Saha & Williams 2001; Raychaudhury et al. 2003): (a) formulating lens reconstruction as an undetermined linear inverse problem, (b) searching through model space to infer H_0 (or alternatively, predict time delays) together with systematic uncertainties, (c) predicting the main features of any Einstein ring, and if observed, estimating the size of the host galaxy. But more importantly, we introduce and

implement two new ideas: (i) reconstructing several time-delay lenses simultaneously while requiring them to agree about H_0 , (ii) making the software so portable that it can be run inside a web browser while reading this paper.

The results in this paper are from two worked examples of seven lenses in all.

1. First we model the time-delay quads 1115+080 and 1608+656, and the ‘dec’ 1933+503. The two time-delay lenses help check against our earlier work using a different code. By coupling them with 1933+503 we can predict time-delays for the latter that are not conditional on H_0 . We also obtain

$$H_0^{-1} = 14.6^{+9.4}_{-1.7} \text{ Gyr} \quad (H_0 = 67^{+9}_{-26} \text{ local units}) \quad \text{at 90\% confidence.}$$

2. Then we model the time-delay doubles 1520+530, 1600+434, 1830-211, and 2149-275, and here the main result

$$H_0^{-1} = 14.5^{+3.3}_{-1.5} \text{ Gyr} \quad (H_0 = 67^{+8}_{-13} \text{ local units}) \quad \text{at 90\% confidence}$$

The reference cosmology has ($\Omega_M = 0.3, \Omega_\Lambda = 0.7$). Note that the two worked examples contain no lenses in common, so the close similarity of the two derived values of H_0 (1 and 2 above) is very encouraging.

The well-known correlations—(i) steeper lenses give higher H_0 , and (ii) more mass in the annulus covering the images gives lower H_0 —are present for most of the lenses, and of these (ii) is better. However, such simple correlations appear to get weaker as H_0 is better constrained, which happens as a consequence of coupling lenses.² Furthermore, lenses with no time delays, like 1933+503, as well as lenses with very asymmetric mass distributions, like 1608+656, are not expected to show the above correlations.

At this stage we remain somewhat cautious about the Hubble-time estimates. As we explained in subsection 2.2, the distribution of models we obtain is conditional on the prior we use. In the past, when the uncertainties on the Hubble time were very large, fine-tuning the prior was not so important. But now, with the uncertainties shrinking down from better data and improved modeling, improving the prior is probably the next priority.

A. Units

In lensing the Hubble time H_0^{-1} plays a more fundamental role than the Hubble constant H_0 . Note that the crucial observable has the same dimensions as H_0^{-1} even though its value is many orders of magnitude different.

²A famous comment by R.O. Redman [quoted by Hogg & Hut (2003)] comes to mind: hearing “after all, a star is a pretty simple thing,” Redman retorted “at a distance of 10 parsecs *you’d* look pretty simple”.

Accordingly, rather than using the traditional dimensionless number h we adopt a dimensionless number g , which is defined by

$$H_0^{-1} = g \text{ Gyr}. \quad (\text{A1})$$

Numerically, $g = 9.78/h$.

To obtain convenient units for the computations, we define

$$T(z_L, z_S) \equiv (1 + z_L) \frac{D_L D_S}{c D_{LS}} \quad (\text{A2})$$

where the distances are computed using a fiducial value $H_0^{-1} = 1 \text{ Gyr}$ (and in some chosen cosmological model). Multiplying further by $3.6525 \times 10^{11}/206265^2$ converts $T(z_L, z_S)$ to units of days arcsec⁻². Then, by using $T(z_L, z_S)$ in appropriate places we can leave all positions in arcsec and all time delays in days.

We remark that in currently-favored cosmological models, H_0^{-1} is nearly equal to age of the universe. In a flat cosmology containing only matter and dark energy, the Hubble time is related to the age by (cf. equation 5.63 in Peebles (1993)).

$$H_0 \times [\text{age}] = \int_0^1 \left(\frac{a}{\Omega_M + (1 - \Omega_M)a^3} \right)^{1/2} da. \quad (\text{A3})$$

If $\Omega_M = 0.3$ then $H_0^{-1} = 0.965 [\text{age}]$. For $\Omega_M \simeq 0.262$ the Hubble time would equal the age; in other words, the current expansion rate would equal the historic mean.

REFERENCES

- AbdelSalam, H.M., Saha, P., & Williams, L.L.R., 1998, AJ, 116, 1541
- Barkana, R, 1997, ApJ, 489, 21
- Biggs, A. D., Browne, I. W. A., Helbig, P., Koopmans, L. V. E., Wilkinson, P. N., Perley, R. A. 1999, MNRAS, 304, 349
- Binney, J., Gerhard, O. E., Stark, A. A., Bally, J. & Uchida, K. I. 1991, MNRAS, 252, 210
- Burud, I. et al. 2000, ApJ, 544, 117
- Burud, I. et al. 2002, A&A, 383, 71
- Burud, I. et al. 2002, A&A, 391, 481
- Chavushyan, V.H., Vlasjuk, V.V., Stepanian, J.A., Erastova, L.K. 1997, A&A, 318, L67
- Cohen, A.S., Hewitt, J.N., Moore, C.B., Haarsma, D.B. 2000 ApJ, 545, 578
- Courbin, F., Meylan, G., Kneib, J.-P. & Lidman, C. 2002, ApJ, 575, 95
- Fassnacht, C.D., Xanthopoulos, E., Koopmans L.V.E., Rusin D. 2002, ApJ, 581, 823
- Gerhard, O., Kronawitter, A., Saglia, R. P., Bender, R. 2001, AJ, 121, 1936
- Heggie, D.C. & Hut, P. 2003, *The Gravitational Million-Body Problem*, Cambridge University Press.
- Hjorth, J. et al. 2002, ApJ, 572, L11
- Impey, C.D., Falco, E.E., Kochanek, C.S., Lehár, J., McLeod, B.A., Rix, H.-W., Peng, C.Y., & Keeton, C.R. 1998, ApJ, 509, 551
- Jackson, N., et al. 1995, MNRAS, 274, L25
- Keeton, C.R. 2001, *gravlens*, available at cfa-www.harvard.edu/glensdata
- Keeton, C.R., & Winn, J.N. 2003, ApJ, 590, 39
- Kochanek, C.S., Falco, E.E., Impey, C., Lehár, J., McLeod, B., Rix, H.-W. 1998, cfa-www.harvard.edu/glensdata
- Kochanek, C.S. 2002, ApJ, 578, 25
- Koopmans, L.V.E. & de Bruyn, A.G. 2003, preprint, astro-ph/0311567
- Knuth, D.E. 1992, *Literate Programming*, CSLI publications.
- Lehar, J. et al. 2000, ApJ, 536, 584

- Lovell, J.E.J., Jauncey, D.L., Reynolds, J.E., Wieringa, M.H., King, E.A., Tzioumis, A.K., McCulloch, P.M., Edwards, P.G., 1998, *ApJ*508, L51
- Myers, S.T. et al. 1995, *ApJ*, 447, 5
- Oscosz, A., et al. 2001, *ApJ*, 552, 81
- Peebles, P.J.E. 1993, *Principles of Physical Cosmology*, Princeton
- Rao, A., & Subrahmanyam, R. 1988, *MNRAS*, 231, 229
- Raychaudhury, S., Saha, P. & Williams, L.L.R. 2003, *AJ*, 126, 29
- Rix, H.-W., de Zeeuw, P. T., Cretton, N., van der Marel, R. P., Carollo, C. M. 1997, *ApJ*, 488, 702
- Saha, P. 2003, *Principles of Data Analysis*, Cappella Archive.
- Saha, P., & Williams, L.L.R. 1997, *MNRAS*, 292, 148
- Saha, P., & Williams, L.L.R. 2001, *AJ*, 122, 585
- Saha, P., & Williams, L.L.R. 2003, *AJ*, 125, 2769
- Schechter P.L. et al. 1997, *ApJ*, 475, L85
- Sykes, C.M. et al. 1998, *MNRAS*, 301, 310
- Trotter, C.S., Winn, J.N., Hewitt, J.N. 2000, *ApJ*, 535, 671
- Young, P., Gunn, J.E., Oke, J.B., Westphal, J.A., Kristian, J. 1981, *ApJ*, 244, 736
- Weymann, R.J. 1980, *Nature*, 285, 641
- Williams, L.L.R. & Saha, P. 2000, *AJ*, 119, 439
- Winn, J.N., Kochanek, C.S., McLeod, B.A., Falco, E.E., Impey, C.D. & Rix, H.-W. 2002, *ApJ*, 575, 103
- Wisotzki, L., Koehler, T., Lopez, S., & Reimers, D. 1996, *A&A*, 315, L405

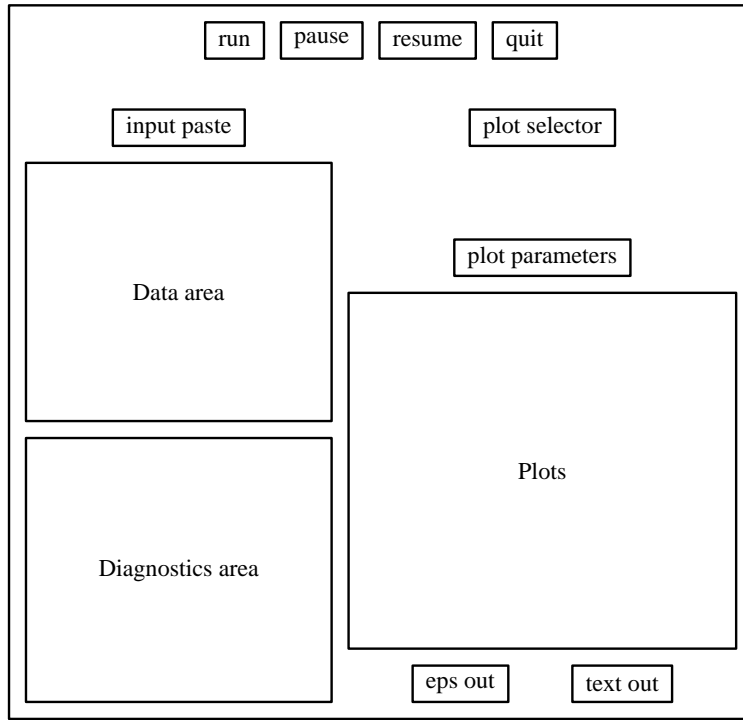


Fig. 1.— The appearance of the *PixeLens* user interface, with all the areas marked.

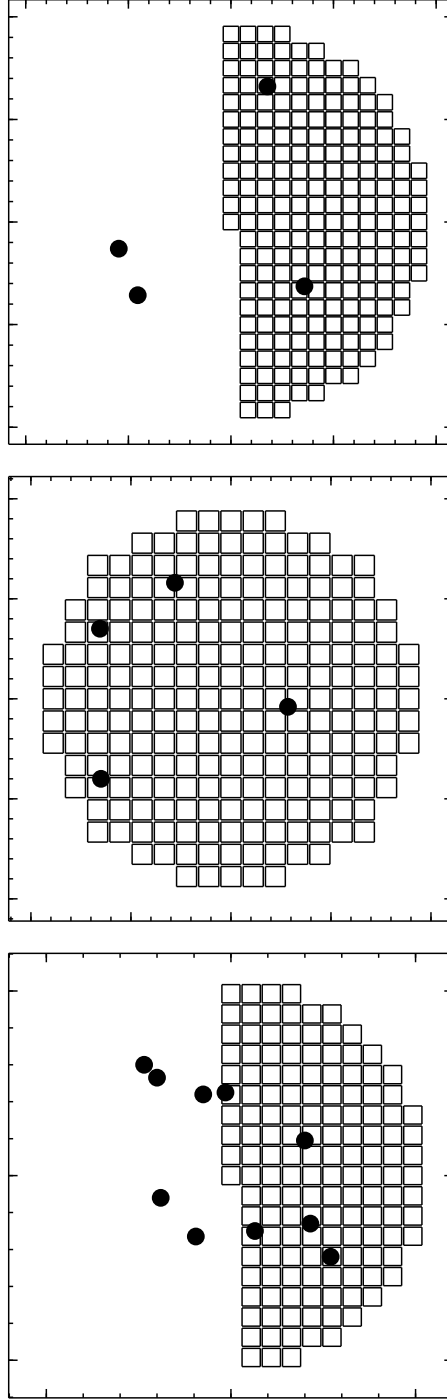


Fig. 2.— Image positions and pixelation for the three lens systems: 1115+080 (upper), 1608+656 (middle), and 1933+503 (lower).

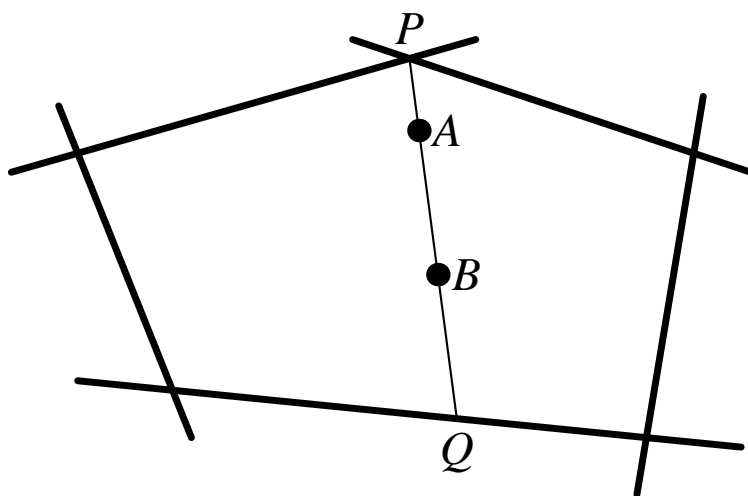


Fig. 3.— Illustration of the Monte-Carlo procedure. The thick lines represent inequality constraints, and any point in the pentagonal region enclosed by these lines is an allowed solution. Suppose we are at solution point A . We now do the following. (1) Choose a random vertex P of the allowed region. (2) Draw the line PQ by drawing PA and extending it to end of the allowed region. (3) Choose a random point B on PQ , and move to it. The roles of A and B in this sequence of operations is symmetric. Hence the probability of moving $A \rightarrow B$ equals the probability of move $B \rightarrow A$.

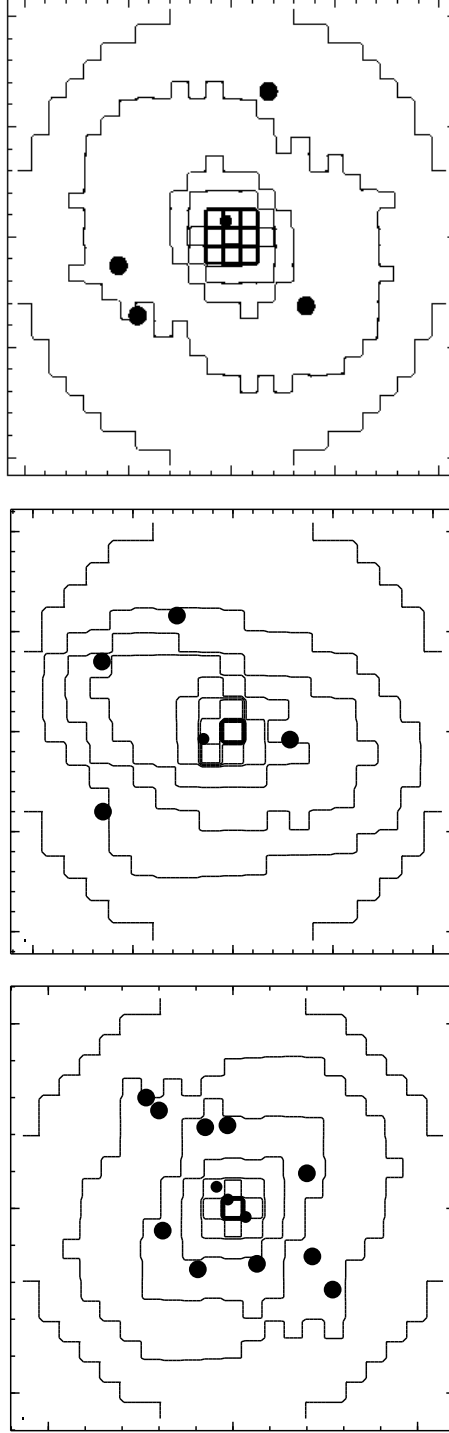


Fig. 4.— Ensemble-average mass maps for the three lenses. The contours are in steps of $\kappa = \frac{1}{3}, \frac{2}{3}, \dots$. The large filled circles are the image positions. The small filled circles near the centres are the inferred source positions.

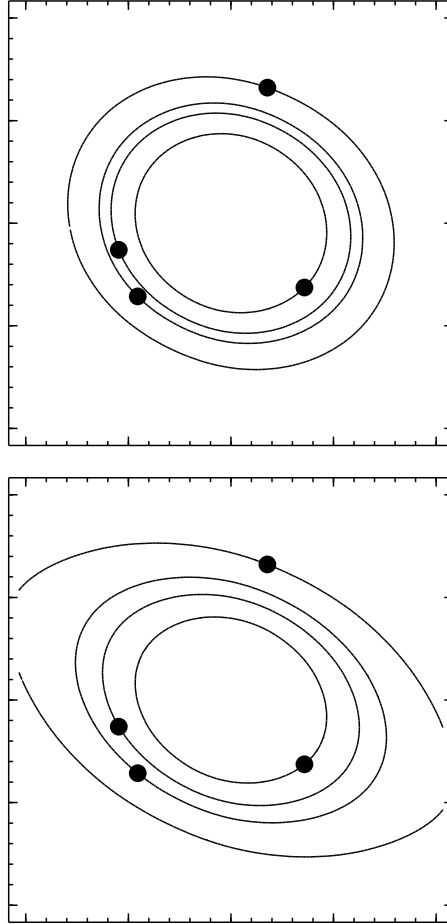


Fig. 5.— Ensemble-average lens potential for 1115+080. Upper panel: Contours of constant ψ , the contours shown being the ones passing through the images. Lower panel: Like the upper panel, but with the external shear exaggerated by a factor of 3.

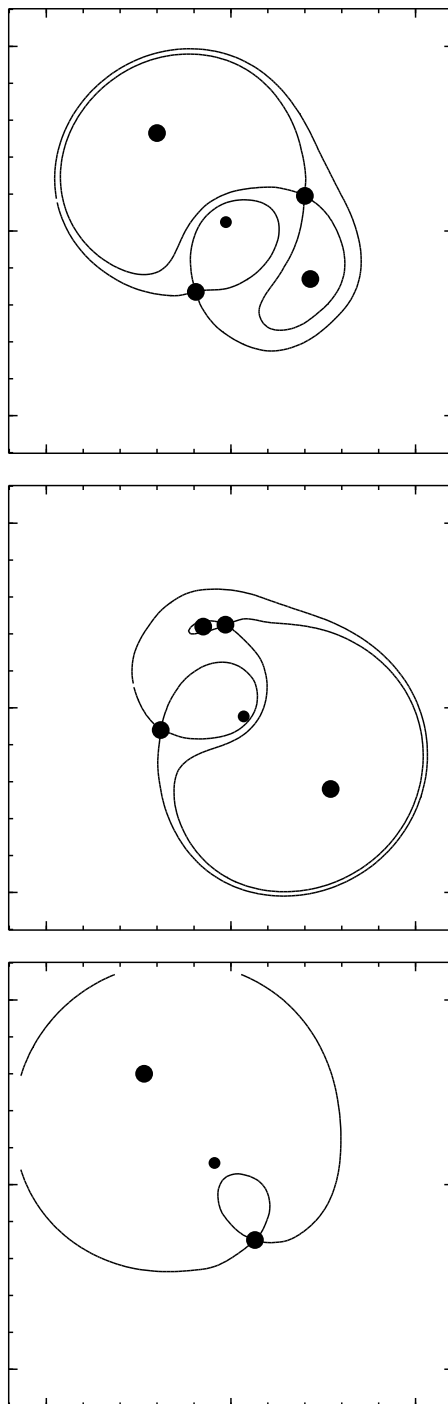


Fig. 6.— Ensemble-average arrival times for the three image systems in 1933+503: core quad (upper), lobe quad (middle), and lobe double (lower). Only the saddle-point contours are shown.

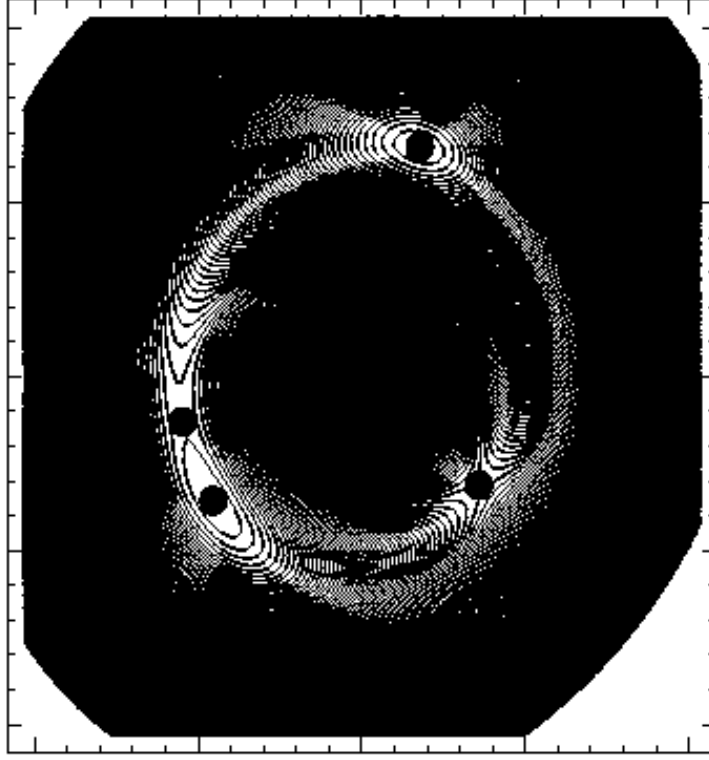


Fig. 7.— Arrival-time surface for 1115+080, with contours spaced by 0.005 arcsec^2 . This represents a simple model of the Einstein ring formed by the host galaxy.

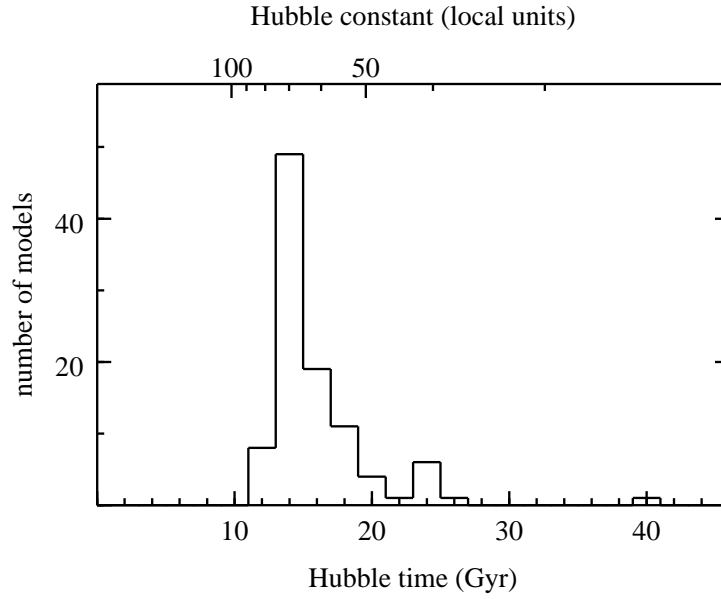


Fig. 8.— Histogram of the Hubble time from 100 three-lens models.

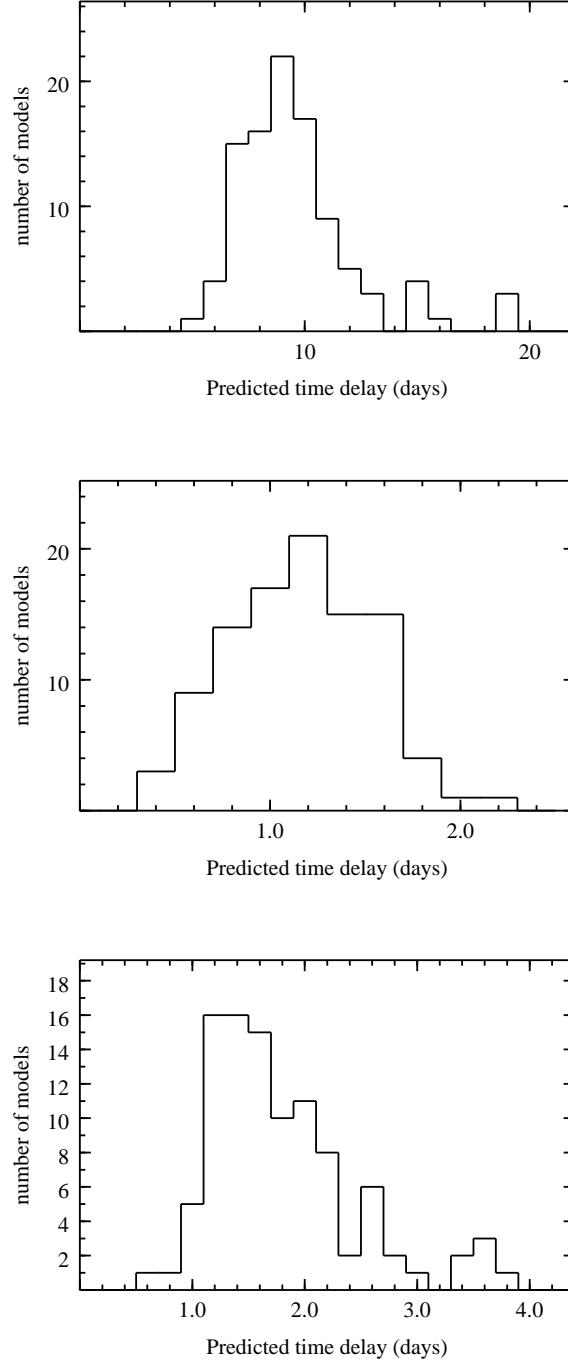


Fig. 9.— Time-delay predictions for the core quad in 1933+503: between images 1 and 2 (upper panel), between 2 and 3 (middle), and between 3 and 4 (lower). See Saha & Williams (2003) for an explanation of how to number images based on arrival times.

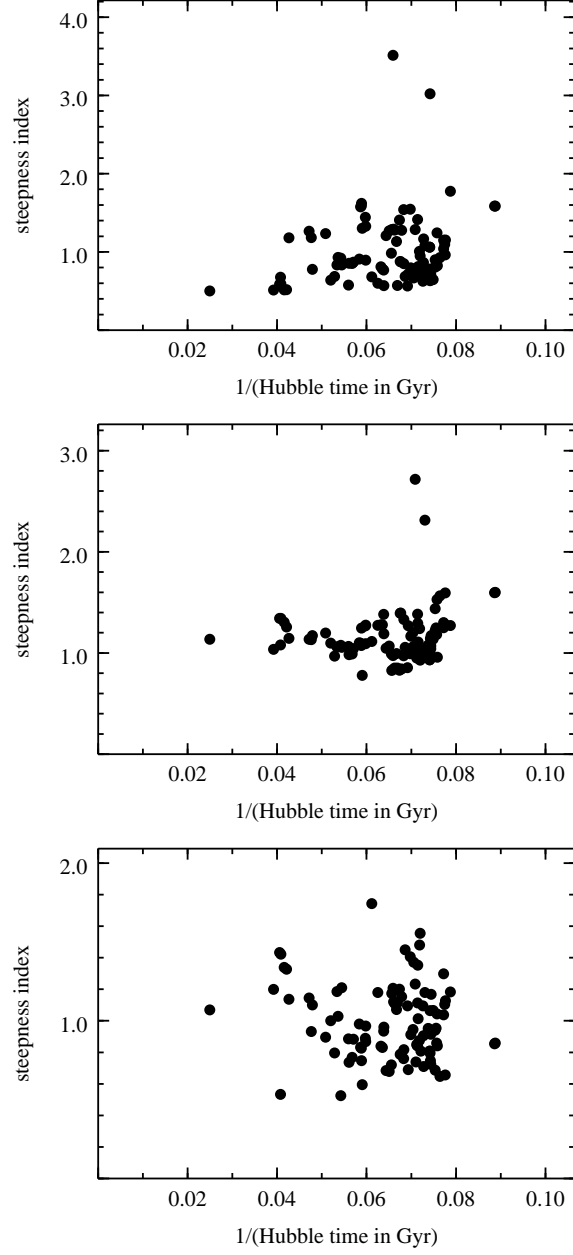


Fig. 10.— Steepness index α against g , for 1115+080 (upper panel), 1608+656 (middle), and 1933+503 (lower). The upper and middle panels are analogous to Figures 13a and 16a respectively in Williams & Saha (2000), except for an obvious change of sign.

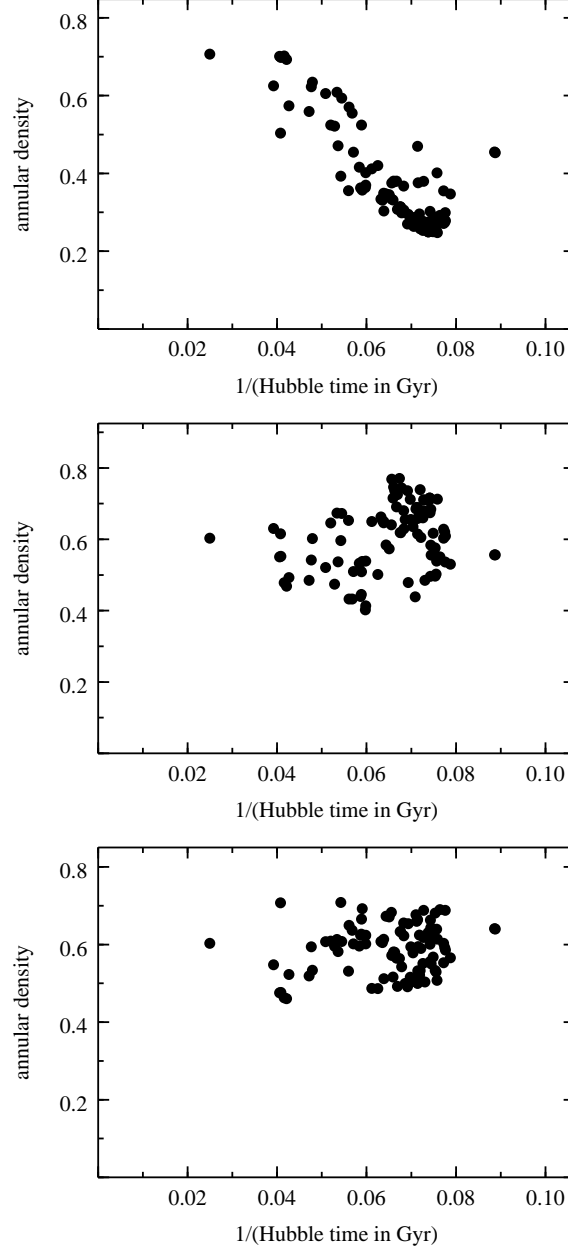


Fig. 11.— Annular density $\langle\kappa\rangle_{\text{ann}}$ against g^{-1} , again for 1115+080 (upper panel), 1608+656 (middle), and 1933+503 (lower).

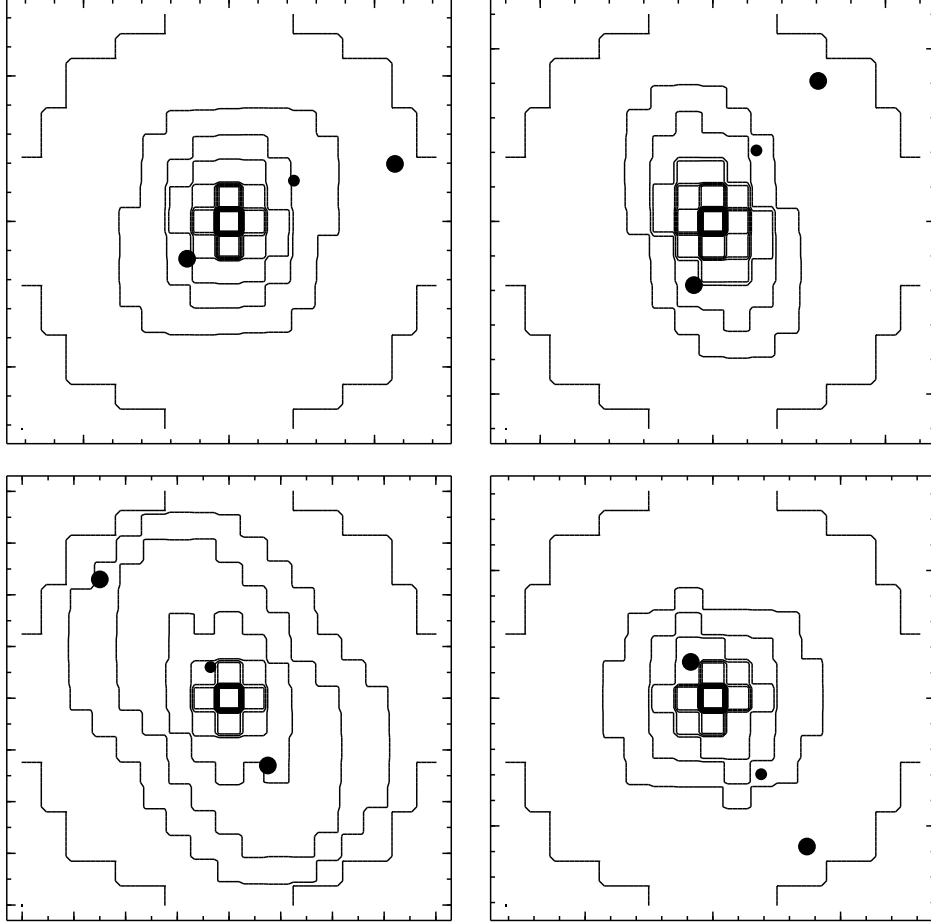


Fig. 12.— Mass maps as in Figure 4, but for 1520+530 (upper left), 1600+434 (upper right), 1830-211 (lower left), and 2149-275 (lower right).

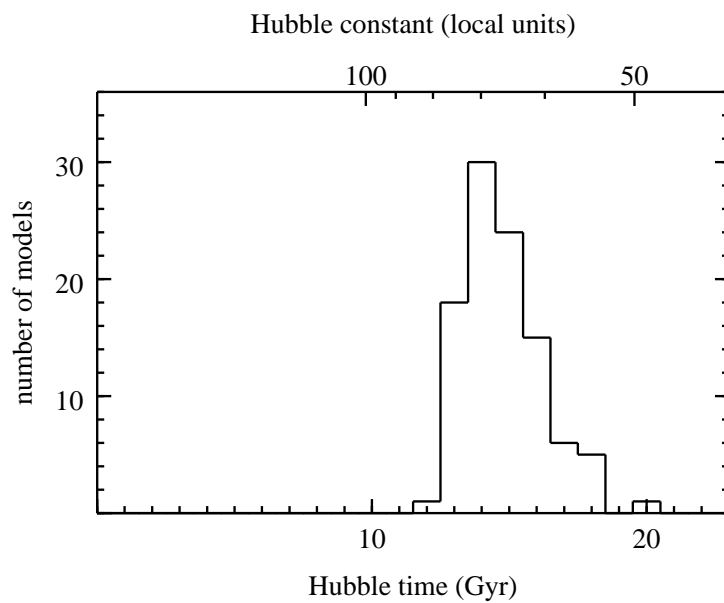


Fig. 13.— Histogram of the Hubble time from 100 four-lens models of 1520+530, 1600+434, 1830-211, and 2149-275.

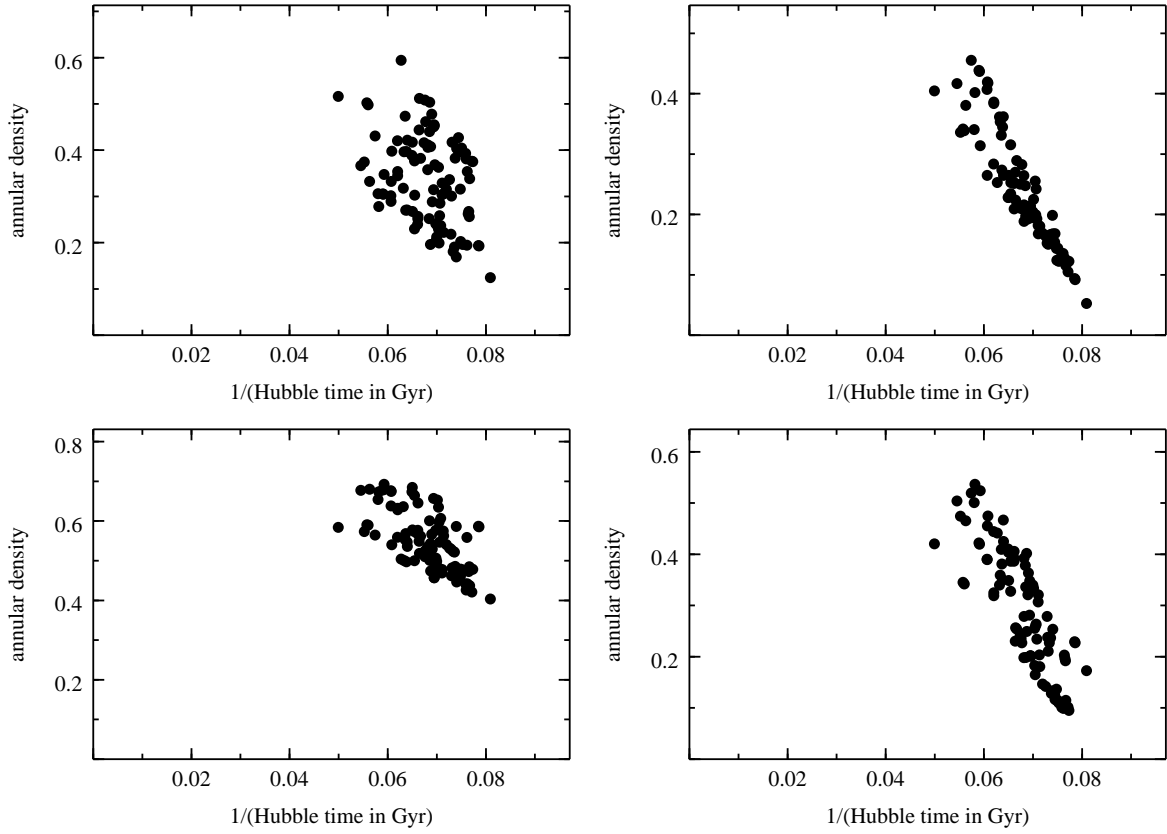


Fig. 14.— Annular density $\langle \kappa \rangle_{\text{ann}}$ as in Figure 11, but for 1520+530 (upper left), 1600+434 (upper right), 1830-211 (lower left), and 2149-275 (lower right).

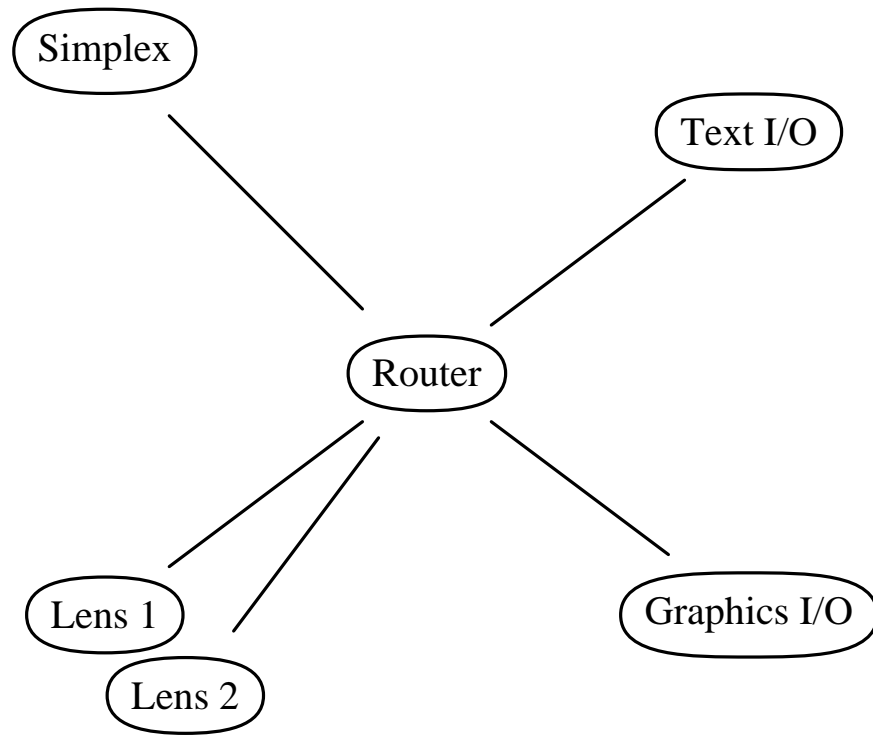


Fig. 15.— Schematic representation of how the code in *PixeLens* is organized.